J Mater Sci: Mater Electron (2018) 29:2301–2306
DOI 10.1007/s10854-017-8146-1

Intrinsic mechanism in nonvolatile polycrystalline zirconium oxide sandwiched structure

Yafei Yuan[1] · Xinran Cao[1] · Yan Sun[2] · Jing Su[1] · Chunmin Liu[1] · Ling Cheng[1] · Yaopeng Li[1] · Lihua Yuan[1] · Hao Zhang[1,3] · Jing Li[1,3]

Received: 25 July 2017 / Accepted: 26 October 2017 / Published online: 3 November 2017
© Springer Science+Business Media, LLC 2017

Abstract Based on the ZrO_2 core layer, two kinds of resistive memory cells with Ag/ZrO_2/Ag and Ag/ZrO_2/ITO sandwiched structures were prepared by a magnetron sputtering system. After thermal treatment, the sample cells show the stable bipolar resistive switching characteristics at room temperature in the current–voltage measurements. The intrinsic mechanism can be well interpreted by the space charge limited conduction effect with charged defects. Two different types of bottom electrode Ag and ITO showed different characteristics. The excellent resistive switching characteristics in the sandwiched structure with ZrO_2 core layer makes it to be a promising candidate for the nonvolatile storage and programmable analog circuit applications.

1 Introduction

Memristors is the fourth fundamental element theoretically proposed by Chua [1], which is a promising solution to traditional memory technologies facing the physical limit. Due to their simple structure, excellent scalability, high switching speed, remarkable endurance, low energy consumption and production cost [2], wide applications in nonvolatile memory [3, 4], logic operation [5], neuromorphic circuits [6], programmable analog circuits [7], great progress has been made, since the first Pt/TiO_2/Pt device was experimentally realized by HP Laboratories [8]. The memristive behaviors were confirmed to exist in various materials such as transition metal oxide [9], perovskite oxides [10], chalcogenides [11, 12], organic materials [13], ferroelectric materials [14] and even the graphene-based structures [15]. The resistive switching (RS) mechanisms have been extensively studied, mainly including ionic migration and pure electronic effect [16]. However, most of the time, the RS process may be very complex, which is related to probably a combination of ionic effect, electronic effect, and even thermal effect. Realizing the intrinsic mechanism is a key for controlling RS accurately, which is beneficial for the development of memristors.

As one of transition metal oxides, ZrO_2 is one of the most promising candidates for SiO_2 replacement which has been researched for RS characteristics [4, 9, 17–22]. Although sufficient studies had been done for the ZrO_2-based memristor, they were mostly about amorphous ZrO_2 film as the insulator layer, and the polycrystalline ZrO_2-based memristor is still seldom investigated. Thus, a deep understanding of the intrinsic RS mechanism in the polycrystalline ZrO_2 core layer is quite important for the future memristive application.

In this paper, we fabricated memristive cells with both Ag/ZrO_2/ITO and Ag/ZrO_2/Ag metal–insulator–metal (MIM) structures by the magnetron sputtering method. The results show that the devices exhibited the intrinsic memristive characteristics. The intrinsic RS mechanism can be well interpreted by the space charge limited conduction (SCLC) effect.

✉ Jing Li
lijing@fudan.edu.cn

1 Department of Optical Science and Engineering, Fudan University, Shanghai 200433, China

2 Shanghai Institute of Technical Physics, Chinese Academy of Sciences, Shanghai 201204, China

3 Shanghai Ultra-Precision Optical Manufacturing Engineering Center, Shanghai 200433, China

2 Experimental

Two kinds of resistive cells with Ag/ZrO_2/Ag and Ag/ZrO_2/ITO sandwiched structures were prepared by a magnetron sputtering system at room temperature. The background vacuum and working pressure are approximately 7×10^{-6} and 2.8×10^{-3} mbar, respectively. The two MIM structural cells with three layers were deposited on the SiO_2/Si(100) substrates. All thickness of each layer including Ag, ZrO_2 and ITO is obtained about 100 nm by controlling the deposition times during the sputtering. Then, all samples were annealed for 45 min in flowing nitrogen atmosphere at 300 °C. The crystallinity of all samples was measured by X-ray diffractometer (Bruker D8 Advance) with Cu-Kα (λ = 1.54056 Å) radiation. The diffraction angles were set from 20° to 60° at 0.02° interval with lasting 3 s in each step. The microstructure was characterized by field emission scan electron microscopy (FESEM). The semiconductor parameter analyzer (Agilent B2912A) was employed to measure the spectral and electronic characteristics respectively.

3 Results and discussion

The structural analysis on the annealed samples with ZrO_2 core layer by the X-ray diffraction is shown in Fig. 1. The observed (−111), (211), (220) and (013) diffraction peaks are identified as ZrO_2 monoclinic structure, which are in good agreement with standard data (JCPDS 37-1484) [23]. The XRD figures show sharp patterns which reveal highly polycrystalline of the ZrO_2 core layer with a preferential orientation (−111) at around 28.4°. The cross sectional SEM image of the Ag/ZrO_2/Ag cell, as shown in the inset of Fig. 1, gives that all the thicknesses of the ZrO_2 core layer, bottom and top electrode layers are about 100 nm respectively.

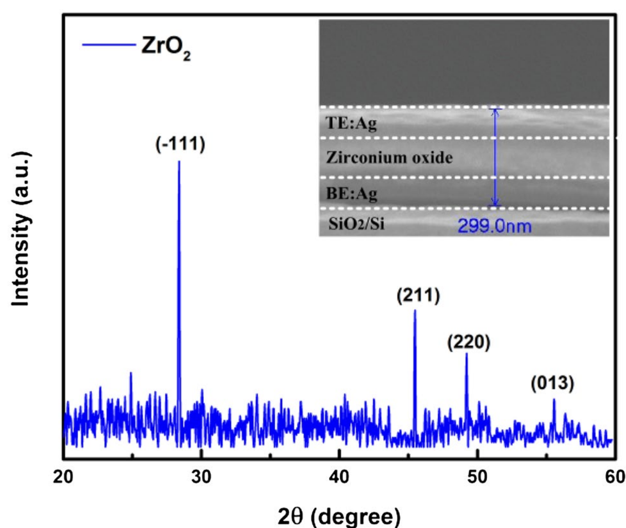

Fig. 1 The XRD pattern of the ZrO_2 film, the inset shows a cross sectional SEM image of Ag/ZrO_2/Ag

The typical current–voltage (*I–V*) characteristics of Ag/ZrO_2/(ITO, Ag) resistive cells with a current compliance of 100 mA are shown in Fig. 2, and the arrows indicate the sweeping directions (step 1 → step 2 → step 3 → step 4). The bipolar RS behavior was observed for all cells and no electrical forming process with a high voltage was needed. The *I–V* characteristics of the sample is shifted from a high resistance state (HRS) to a low resistance state (LRS) by a positive bias sweep, known as the SET process. Then, the sample cell returns to HRS by a negative bias sweep, known as the RESET process. As shown in Fig. 2a, the threshold voltage in the positive and negative regions for the Ag/ZrO_2/ITO sample cell is approximately 1.8 V (SET) and − 0.7 V (RESET), respectively. The cell exhibits stable bipolar resistive switching behavior during the 100 cycles loop subsequent voltage sweeping process from 2 to − 2 V, as shown in Fig. 2b. Then, the Ag bottom electrode instead of the ITO bottom electrode, the *I–V* characteristic of Ag/ZrO_2/Ag sample exhibits a little different characteristic. Figure 2c reveals that the threshold voltage in the positive and negative regions for the Ag/ZrO_2/Ag cell are approximately 1.5 V (SET) and − 1.5 V (RESET) respectively. Figure 2d shows that the sample exhibits stable bipolar RS behavior during the 100 cycles loop subsequent voltage sweeping process from 2 to − 2 V. It is obvious that the resistance of Ag/ZrO_2/ITO cell is much higher than that of the Ag/ZrO_2/Ag cell in HRS because Ag is an active electrode while ITO is an inert electrode. Besides, the resistance of both devices are similar in LRS which should be due to the similar RS mechanism. The sample cell with ITO bottom electrode exhibits an asymmetric behavior of *I–V* characteristics while another cell with Ag bottom electrode shows symmetry. The resistance of Ag/ZrO_2/Ag sample cell changes continuously rather than an abrupt jump compared with Ag/ZrO_2/ITO cell, which can be attributed to the conduction mechanism.

As we know, there are several conduction mechanism models [6, 16], i.e. Schottky emission, Poole–Frenkel emission (P–F), Fowler–Nordheim tunneling (F–N), SCLC and so on, which can be used to describe the physics of nonlinear *I–V* characteristics. It is necessary to distinguish these conduction mechanisms, because there should be several conduction mechanisms contributing to the device conduction current at the same time.

In order to discuss the conduction mechanism of Ag/ZrO_2/ITO cell, the *I–V* curves have been replotted using log scale, as shown in Fig. 3. Figure 3a shows that the SCLC mechanism is suitable to account for the conducting features at the HRS within positive voltage region. The slope of HRS is very close to linear at the low voltage region, which corresponds to the Ohmic law region

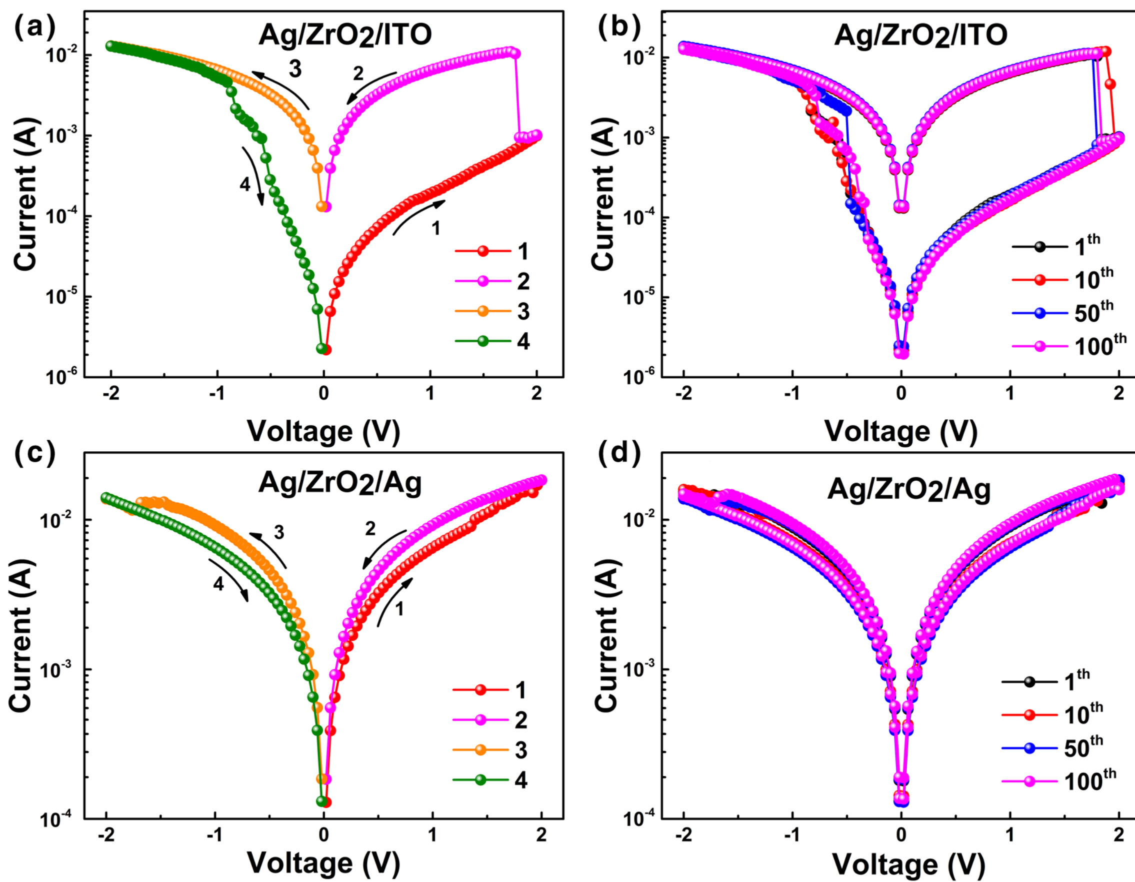

Fig. 2 **a** Typical bipolar *I*–*V* characteristic of Ag/ZrO_2/ITO in sweeping DC voltages. **b** The *I*–*V* characteristic of Ag/ZrO_2/ITO for a certain times cycles. **c** Typical bipolar *I*–*V* characteristic of Ag/ZrO_2/Ag in sweeping DC voltages. **d** The *I*–*V* characteristic of Ag/ZrO_2/Ag for a certain times cycles

($I \propto V$). At the voltages larger than SET voltage (1.8 V), the current follows square dependence on voltage in HRS, corresponding to the Child's square law region ($I \propto V^2$). The current density for trap-controlled SCLC emission can be expressed as follows [20],

$$J = \left(\frac{\theta}{\theta + 1}\right)\frac{9\mu\varepsilon_r\varepsilon_0 V^2}{8L^3}$$

where J is the current density, $\theta = \left(N_c/N_t\right)e^{-(E_c-E_t)/k_BT}$ is the ratio of free electron to trapped electron, N_c is the effective density of states in the conductive band, $N_t$is the number of emptied electron traps, k_B is the Boltzmann constant, ε_r is the static dielectric constant, ε_0 is the permittivity of frees pace, μ is the electron mobility, V is the applied voltage and L is the film thickness. In the low voltage region, when the density of thermally generated free electrons inside the cell is greater than that of the injected electrons from the electrode, the majority of electron traps are emptied ($\theta \ll 1$). The *I*–*V* characteristics of the cell are mainly affected by the Ohmic emission mechanism. Thus, the current density equation can be given,

$$J = \theta\frac{9\mu\varepsilon_r\varepsilon_0 V^2}{8L^3}$$

In the strong injections process, the increase of applied voltage may increase the density of free carriers resulting from lifting up Fermi level well above the electron trapping level. Then, the majority of electron traps are occupied ($\theta \gg 1$), showing that the density of injected electrons gradually exceeds the thermal equilibrium concentration in the cell. The injected electrons affect mainly the *I*–*V* characteristics of the cell, and the *I*–*V* relationship obeys the square law. In this case, the current density equation can be given,

$$J = \frac{9\mu\varepsilon_r\varepsilon_0 V^2}{8L^3}$$

It is observed that the resistance changed abruptly from HRS to LRS. This abrupt change is related to the trap

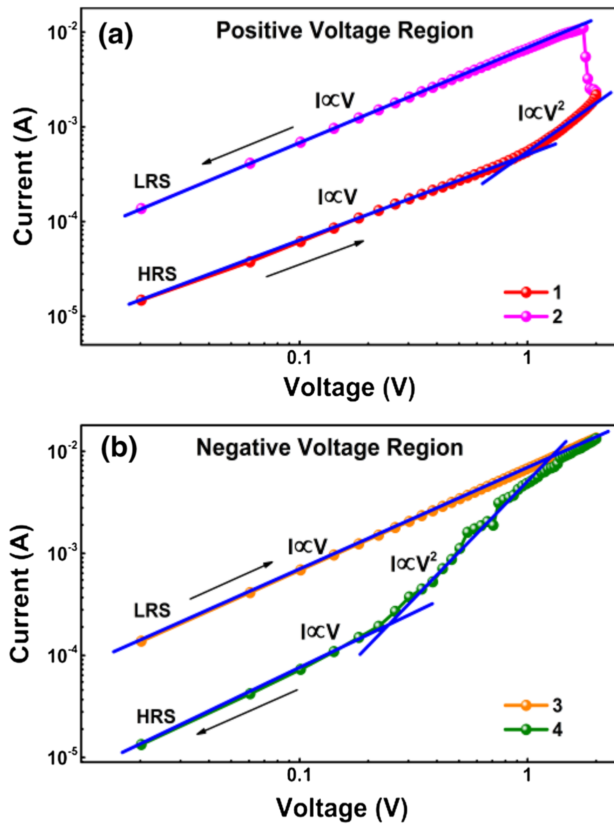

Fig. 3 **a** The *I–V* curve of Ag/ZrO_2/ITO at positive voltage region. **b** The *I–V* curve of Ag/ZrO_2/ITO at negative voltage region

distribution. The exponential distribution of traps can be described by the expression as follows [11],

$$D(E) = \frac{N_t}{k_B T_c} \exp\left(-\frac{E - E_v}{k_B T_c}\right)$$

where $D(E)$ is the trap density per unit energy range at an energy E above the valance band edge, N_t is the total density of traps, and N_t/kT_c is the trap at the valence band edge, T_c is the characteristic temperature.

Generally, the defects in the polycrystalline chalcogenide can be divided into two types: (i) defects within the crystalline grain, (ii) defects at the grain boundaries arising from dangling bonds. These defects form localized states near the valence band, which can act as charge traps and absorb injected carriers [24]. The resistance states depend on the carrier trapping levels in the device, namely the high trapping level corresponding to LRS while the low one corresponding to HRS. The resistance exhibits LRS when the deep traps are filled totally.

It is noted that the LRS of cell in positive voltage region can be best fitted with Ohmic law during the sweep voltage of 2 V → 0 V due to the formation of Ag filament, which is consistent with other works [19, 22]. The formation process can be described as follows. When the top electrode of Ag is applied with a positive bias voltage, Ag atoms are oxidized to Ag ions according to $Ag \rightarrow Ag^+ + e$. When the electric field in the ZrO_2 layer film is strong enough, these Ag ions will migrate toward the ITO electrode, where they are reduced back to metallic Ag atoms according to $Ag^+ + e \rightarrow Ag$. The metallic Ag filament finally reaches the Ag electrode when the process reaches SET voltage. Meanwhile, the resistance of the cell drops abruptly, leading to LRS. Thus the LRS cell shows the Ohmic conduction behavior. In this case, the current density of Ohmic conduction can be expressed as follows [16],

$$J = \sigma E = \frac{nq\mu V}{L}$$

where σ is electrical conductivity, n is the number of electrons in the conduction band, μ is electron mobility, V is the applied voltage. In negative bias voltage region, the transition from LRS to HRS state occurs at the RESET voltage (− 0.7 V) during the sweep voltage of − 2 V → 0 V. The filament is ruptured by Joule heat assistance during the negative voltage sweep. While the occupied trap will discharge the electrons and the current reduces quickly. The device maintains HRS until the majority of cell traps is emptied.

In order to understand different bottom electrode effects, the *I–V* curves of Ag/ZrO_2/Ag cell have been replotted using log scale, as shown in Fig. 4. The result is similar to the behavior of the Ag/ZrO_2/ITO cell. The conduction behavior obeys SCLC mechanism conduction and Ohmic law. In the positive voltage region, the *I–V* curves shows linear ($I \propto V$) behavior under low voltage. At the voltage larger than SET voltage (1.5 V), the current of HRS follows square dependence on voltage due to the Child's law ($I \propto V^2$). The resistance of Ag bottom electrode belonging to strong current injection changes continuously into LRS which is distinguish with the ITO bottom electrode belonging to weaken current injection. The current value of the Ag/ZrO_2/Ag cell is close to the Ag/ZrO_2/ITO cell in the LRS which is caused by the same mechanism obeying Ohmic law.

To further investigate the performance of the Ag/ZrO_2/ITO and Ag/ZrO_2/Ag cells, the cycling endurance characteristics were measured in pulse sweep mode for 1000 cycles, respectively, as shown in Fig. 5. The applied plus is 2 V/1 μs for SET process and − 2 V for the RESET process, respectively. The reading voltage is 0.5 V as shown in Fig. 5a. Figure 5b shows the endurance behavior of Ag/ZrO_2/ITO cell for 1000 cycles without margin deterioration. It is obvious that the HRS is more discrete than the LRS due to the more stable LRS of the cell. The resistance ratio between HRS and LRS is at least 32 times large enough for the periphery circuits to probe the different resistance states and the result is better than the previous works [3, 4, 17, 21]. Figure 5c shows the endurance behavior of Ag/ZrO_2/Ag cell for 1000 cycles

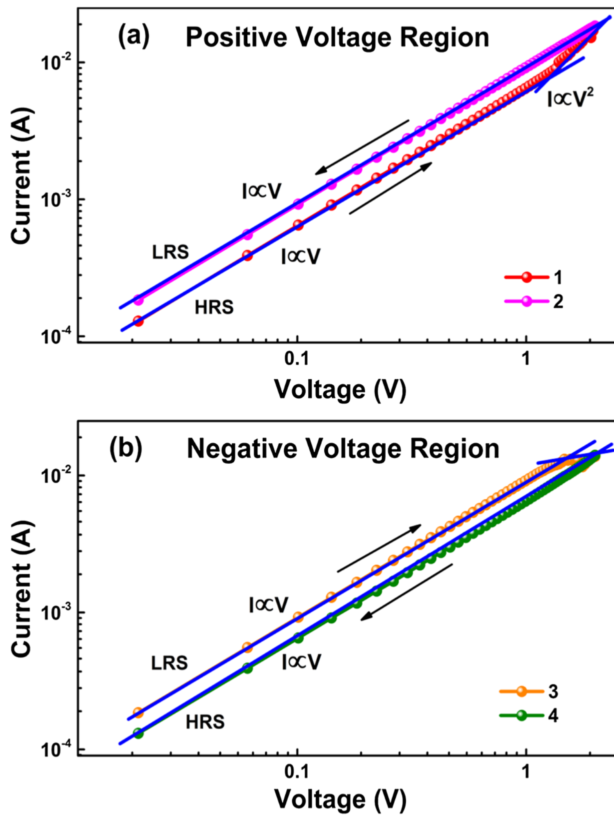

Fig. 4 **a** The *I–V* curve of Ag/ZrO_2/Ag at positive voltage region. **b** The *I–V* curve of Ag/ZrO_2/Ag at negative voltage region

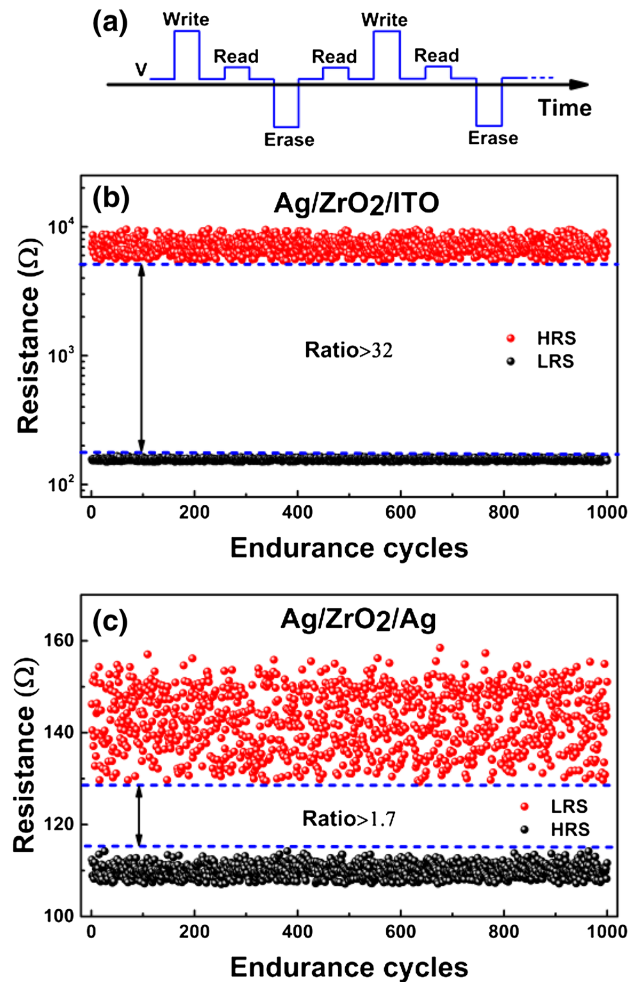

Fig. 5 **a** The plus excitation voltage. **b** The resistance of Ag/ZrO_2/ITO cell for 1000 cycles. **c** The resistance of Ag/ZrO_2/Ag cell for 1000 cycles

without switching failure. It is obvious that the HRS is more discrete than the LRS due to the wide distribution HRS of the cell. The ratio resistance between HRS and LRS is only about 1.7 times not large enough for distinguishing in storage application. This phenomenon should be attributed to the resistance switching conduction mechanism. As the top and bottom electrodes are both Ag electrodes, the resistance switching between HRS and LRS is mainly bound up with SCLC. The filament could not be ruptured owing to the oxidation–reduction reactions of Ag in all the processes during both the positive voltage sweep and negative voltage sweep.

To further confirm the potential memory application of Ag/ZrO_2/ITO cell, the distribution and retention characteristics were investigated. The distribution of the SET and RESET voltages taken over 100 cycles for the device is shown in Fig. 6a. The distributions of SET and RESET voltages were measured to ~0.1 and ~0.3 V, respectively. The RESET voltage distributes wider than the SET voltage. The retention characteristics of both resistance states were investigated under reading voltage of 0.5 V at 85 °C, as shown in Fig. 6b. The resistance of both HRS and LRS exhibit little change, confirming the nonvolatile and nondestructive readout characteristics of this cell, which also may lead to the nonvolatile storage application.

4 Conclusions

In summary, based on the ZrO_2 core layer, two kinds of Ag/ZrO_2/ITO and Ag/ZrO_2/Ag had been successfully prepared using magnetron sputtering method. The XRD analysis shows that the films exhibit good crystalline quality with monoclinic structure. The cross sectional SEM image of the Ag/ZrO_2/Ag cell shows clearly a sandwiched structure. Both the two kinds of sandwich-structure cells with ZrO_2 core layer show bipolar memristive switching behavior and possess the properties of reversible switching, reproducible resistance, nondestructive readout, good cycling performance and nonvolatile. The intrinsic memristive characteristics conforms to the SCLC mechanism caused by the defects in the polycrystalline ZrO_2 core layer. The ITO bottom electrode in the cell shows the higher interface resistance and weak injection that the resistance change is an abrupt jump suitable for storage application, while another cell with Ag

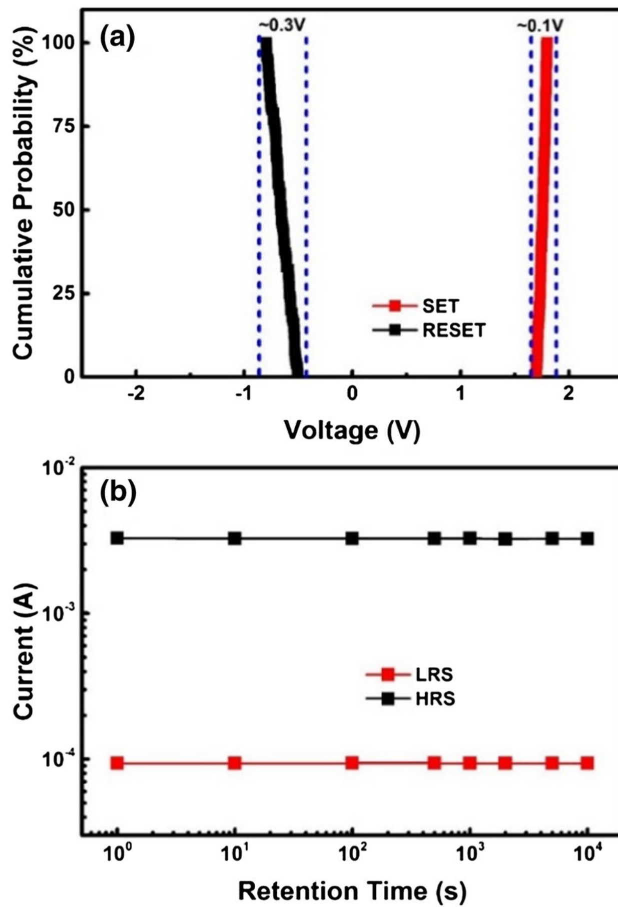

Fig. 6 **a** The probability plots of the SET and RESET voltage distributions for Ag/ZrO_2/ITO cell with 100 cycles. **b** The retention characteristics for Ag/ZrO_2/ITO cell

bottom electrode presents the lower interface resistance and strong injection that resistance change is continuous, which may lead to the neuromorphic circuit application.

Acknowledgements The authors would like to express their sincere thanks for the financial supports by the funding under Grant Nos. 17ZR1402200, 13ZR1402600, 60578047, 61427815 and 2015KF003. The authors thank Prof. L. Y. Chen and Prof. M. Xu for effective backup.

References

1. L.O. Chua, IEEE Trans. Circuit Theory **18**, 507–512 (1971)
2. M. Aljafar, P. Long, M. Perkowski, BioNanoScience **6**, 214–234 (2016)
3. X. Wu, P. Zhou, J. Li, L.Y. Chen, H.B. Lv, Y.Y. Lin, T.A. Tang, Appl. Phys. Lett. **90**(18), 183507 (2007)
4. P. Zhou, J. LI, L.Y. Chen, T. Tang, Y. Lin, Chin. Phys. Lett. **25**, 3742–3745 (2008)
5. A. Siemon, T. Breuer, N. Aslam, S. Ferch, W. Kim, J. van den Hurk, V. Rana, S. Hoffmann-Eifert, R. Waser, S. Menzel, E. Linn, Adv. Funct. Mater. **25**, 6414–6423 (2015)
6. T. Shi, X.B. Yin, R. Yang, X. Guo, Phys. Chem. Chem. Phys. **18**, 9338–9343 (2016)
7. J.X. Zha, H. Huang, Y.J. Liu, IEEE Trans. Circuits Syst. **63**, 423–427 (2016)
8. D.B. Strukov, G.S. Snider, D.R. Stewart, R.S. Williams, Nature **453**, 80–83 (2008)
9. W. Guan, S. Long, R. Jia, M. Liu, Appl. Phys. Lett. **91**, 062111 (2007)
10. R. Muenstermann, T. Menke, R. Dittmann, R. Waser, Adv. Mater. **22**, 4819–4822 (2010)
11. Y. Li, Y.P. Zhong, J.J. Zhang, X.H. Xu, Q. Wang, L. Xu, H.J. Sun, X.S. Miao, Appl. Phys. Lett. **103**, 043501 (2013)
12. V. Kannan, H.-S. Kim, H.-C. Park, J. Mater. Sci. **27**, 3488–3492 (2015)
13. T.W. Kim, H. Choi, S.H. Oh, M. Jo, G. Wang, B. Cho, D.Y. Kim, H. Hwang, T. Lee, Nanotechnology **20**, 025201 (2009)
14. L. Jin, Y. Shuai, H.Z. Zeng, W.B. Luo, C.G. Wu, W.L. Zhang, X.Q. Pan, P. Zhang, Y.R. Li, J. Mater. Sci. **26**, 1727–1731 (2014)
15. M. Rogala, P.J. Kowalczyk, P. Dabrowski, I. Wlasny, W. Kozlowski, A. Busiakiewicz, S. Pawlowski, G. Dobinski, M. Smolny, I. Karaduman, L. Lipinska, R. Kozinski, K. Librant, J. Jagiello, K. Grodecki, J.M. Baranowski, K. Szot, Z. Klusek, Appl. Phys. Lett. **106**, 263104 (2015)
16. F.C. Chiu, Adv. Mater. Sci. Eng. **2014**, 1–18 (2014)
17. T.-L. Tsai, Y.-H. Lin, T.-Y. Tseng, IEEE Electron Device Lett. **36**, 675–673 (2015)
18. P. Parreira, G.W. Paterson, S. McVitie, D.A. MacLaren, J. Phys. D **49**, 095111 (2016)
19. W. Guan, M. Liu, S. Long, Q. Liu, W. Wang, Appl. Phys. Lett. **93**, 223506 (2008)
20. Q. Liu, W. Guan, S. Long, R. Jia, M. Liu, J. Chen, Appl. Phys. Lett. **92**, 012117 (2008)
21. Q. Zuo, S. Long, Q. Liu, S. Zhang, Q. Wang, Y. Li, Y. Wang, M. Liu, J. Appl. Phys. **106**, 073724 (2009)
22. S. Long, Q. Liu, H. Lv, Y. Li, Y. Wang, S. Zhang, W. Lian, K. Zhang, M. Wang, H. Xie, M. Liu, Appl. Phys. A **102**, 915–919 (2011)
23. L. Kumari, G.H. Du, W.Z. Li, R.S. Vennila, S.K. Saxena, D.Z. Wang, Ceram. Int. **35**, 2401–2408 (2009)
24. D.S. Shang, Q. Wang, L.D. Chen, R. Dong, X.M. Li, W.Q. Zhang, Phys. Rev. B **73**, 245427 (2006)